deCLUTTER^{2+} pipeline to analyze calcium traces in a novel stem cell model for ventral midbrain patterned astrocytes

Martyna M. Grochowska[1, *], Federico Ferraro[1, *], Ana Carreras Mascaro[1, †], Domenico Natale[1, †], Amber Winkelaar[1], Valerie Boumeester[1], Guido J. Breedveld[1], Vincenzo Bonifati[1], Wim Mandemakers[1]

[1]Erasmus MC, University Medical Center Rotterdam, Department of Clinical Genetics, P.O. Box 2040, 3000 CA, Rotterdam, Netherlands

[*], [†] contributed equally

Correspondence to: Wim Mandemakers

Corresponding authors' e-mail addresses: w.mandemakers@erasmusmc.nl

Title character count: 17 words, 116 characters (with spaces)

Abstract word count: 182

The number of references: 90

Number of figures/tables: 4 items

Fig. 1 Generation and immunocytochemical characterization of astrocytes from ventral midbrain patterned progenitors

Fig. 2 Transcriptomic characterization of progenitors and astrocytes

Fig. 3 Functional characterization of astrocytes

Fig. 4 Characterization of ATP-induced Ca^{2+} transients in astrocytes

Supplementary Material: 7 items

Supplementary Fig. 1 Generation and characterization of iPSCs and iPSC-derived ventral midbrain patterned progenitors

Supplementary Fig. 2 eSNP-Karyotyping reveals chromosomal multiplication in one astrocyte line

Supplementary Table 1 Differentiation protocols that generate ventral midbrain astrocytes

Supplementary Table 2 Cell culture media composition

Supplementary Table 3 Details of the primary antibodies used in this study

Supplementary Table 4 Details of the 14 stem cell-derived clonal cell lines used in this study

Supplementary Table 5 qPCR primers

Supplementary Table 6 Differential expression analysis results report

Supplementary Table 7 Gene set enrichment analysis results report

Abstract (182 words)

Astrocytes are the most populous cell type of the human central nervous system and are essential for physiological brain function. Increasing evidence suggests multiple roles for astrocytes in Parkinson's disease (PD), nudging a shift in the research focus, which historically pivoted around the ventral midbrain dopaminergic neurons (vmDANs). Studying human astrocytes and other cell types in vivo remains technically and ethically challenging. However, in vitro reprogrammed human stem cell-based models provide a promising alternative. Here, we describe a novel protocol for astrocyte differentiation from human stem cell-derived vmDANs-generating progenitors. This protocol simulates the regionalization, gliogenic switch, radial migration, and final differentiation that occur in the developing human brain. We have characterized the morphological, molecular, and functional features of these ventral midbrain astrocytes with a broad palette of techniques. In addition, we have developed a new pipeline for calcium imaging data analysis called deCLUTTER^{2+} (deconvolution of Ca^{2+} fluorescent patterns) that can be used to discover spontaneous or cue-dependent patterns of Ca^{2+} transients. Altogether, our protocol enables the characterization of the functional properties of human ventral midbrain astrocytes under physiological conditions and in PD.

Keywords

Human astrocytes, ventral midbrain, induced pluripotent stem cells, disease modeling, Parkinson's disease, calcium imaging data analysis, human stem cell-based models

1. Introduction

Astrocytes are specialized glial cells essential for the healthy functioning of the nervous system (Sofroniew and Vinters, 2010). Astrocytes release neurotrophic factors (Dezonne et al., 2013; Gomes et al., 1999; Gomes et al., 2005; Nones et al., 2012), ensure the formation and maintenance of the blood-brain barrier (Verkhratsky and Nedergaard, 2018), regulate brain energy metabolism (Beard et al., 2021; Gonzalez-Reyes et al., 2017), modulate synaptic activity (Chung et al., 2015), and allow the movement of fluid between the

60 paravascular spaces and the interstitium (Jessen et al., 2015). In addition, astrocytes provide metabolic
61 support to neurons, including the uptake and exchange of mitochondria (Scheibye-Knudsen et al., 2015)
62 and lipids (Ioannou et al., 2019; Liu et al., 2015).

63 The accumulating evidence points out that some of these homeostatic and neuronal health-promoting
64 functions of astrocytes are impaired in Parkinson's disease (PD) (Booth et al., 2017; MacMahon Copas et
65 al., 2021). The majority of PD research focusses on the vulnerable ventral midbrain dopaminergic neurons
66 (vmDANs), whose progressive loss is a disease hallmark. In recent years, however, the role of astrocytes in
67 the neurodegenerative processes gained more attention. Studies have shown that genes known to cause
68 inherited forms of PD are highly expressed in astrocytes and play vital roles in astrocyte function
69 (Bandopadhyay et al., 2004a; Bandopadhyay et al., 2004b; di Domenico et al., 2019; Grochowska et al.,
70 2021; Kim et al., 2016; Kim et al., 2013; Qiao et al., 2016; Strokin et al., 2012). Moreover, in PD, astrocytes
71 can acquire a neurotoxic phenotype, enhance neurodegeneration and thus form a target for therapeutic
72 intervention (Liddelow et al., 2017; Miyazaki and Asanuma, 2020; Schonhoff et al., 2020; Yun et al., 2018).

73 Astrocytes are a highly heterogeneous cell type based on their morphology, transcriptome, and physiology
74 (Batiuk et al., 2020; Bayraktar et al., 2020; Oberheim et al., 2009; Pestana et al., 2020; Siletti et al., 2022).
75 They elicit heterogeneous responses to injury and functionally specialize to their surrounding tissue
76 (Bugiani et al., 2022). Astrocytes residing in the ventral midbrain are physiologically distinct from, e.g.,
77 astrocytes in the cortex and hippocampus (Siletti et al., 2022; Xin et al., 2019). Additionally, ventral midbrain
78 astrocytes alleviate neuronal α-synuclein pathology, which is one of the main pathological hallmarks of PD
79 (Yang et al., 2022).

80 Studying specific characteristics of human ventral midbrain astrocytes in PD remains challenging due to
81 limited access to primary human cells from the affected brain regions. However, using induced pluripotent
82 stem cell (iPSC) technology, it is now possible to generate various astrocyte populations of human origin in

83 vitro (Lanjewar and Sloan, 2021). Evidence supports that patterning of iPSC-derived progenitors to rostral-
84 caudal and dorsal-ventral identities with the same morphogens used for the neuronal subtype specification
85 generates region-specific astroglial subtypes (Krencik et al., 2011).

86 A limited number of protocols exists that allows the generation of ventral midbrain astrocytes
87 (**Supplementary Table 1**). A feature shared by these protocols is the generation of progenitor cells patterned
88 toward a mesencephalic fate (floor-plate progenitors) that can also differentiate into vmDANs. Although
89 these models have been an advancement in the PD research field, modifications, and improved
90 characterization remain necessary to generate more accurate models of human ventral midbrain
91 astrocytes.

92 Here, we describe a novel protocol for generating ventral midbrain patterned astrocytes from iPSCs. Similar
93 to previous studies, we rely on the ventral neural tube patterning of iPSC-derived neuroepithelial cells to
94 generate ventral midbrain astrocytes from a population of progenitors that can also produce vmDANs
95 (Reinhardt et al., 2013). Our protocol mimics gliogenesis in vitro, including regionalization, gliogenic switch,
96 radial migration, and final differentiation. In comparison to previous studies, our simplified protocol
97 efficiently generates mature ventral midbrain astrocytes relatively fast, without the use of serum or
98 transgenic reporters, and a limited number of necessary additives. We characterized these astrocytes using
99 immunocytochemistry (ICC), RNA-sequencing (RNA-seq), and a battery of functional assays, including pro-
100 inflammatory cytokine treatment, glutamate uptake, and fluorescence time-lapse calcium confocal
101 imaging. Furthermore, we developed a novel pipeline for the functional analysis of calcium imaging data
102 from in vitro experiments that we named deCLUTTER^{2+} (deconvolution of Ca^{2+} fluorescent patterns).
103 Altogether, our model can potentially study the properties of ventral midbrain astrocytes under
104 physiological conditions and in PD.

105 ## 2. Materials and methods

106 2.1 Primary cell lines

107 We generated eight human iPSC lines (**Supplementary Table 4**). Clonal lines D1-c1-iPSC and D1-c2-iPSC were
108 generated from the commercially available dermal fibroblasts from a female donor (Gibco™, Lot number:
109 1903939). The skin biopsy was sampled at the age of 33. Clonal lines D2-c1-iPSC and D2-c2-iPSC were
110 derived from the commercially available dermal fibroblasts from a female donor (Gibco™, Lot number:
111 181388). The skin biopsy was sampled at the age of 34. Clonal lines D3-c1-iPSC, D3-c2-iPSC, D3-c3-iPSC
112 were generated from the primary fibroblasts from a female donor available in our institute. The skin biopsy
113 was sampled at the age of 68. Line D4-c1-iPSC was derived from the primary cultures of erythroid
114 progenitors (Leberbauer et al., 2005; van den Akker et al., 2010), which were generated from the peripheral
115 blood of a female donor available in our institute. The blood was sampled at the age of 83. All study
116 procedures were approved by the medical ethical committee of Erasmus MC and conformed to the
117 principles of the WMA Declaration of Helsinki and the Department of Health and Human Services Belmont
118 report. Participating subjects provided written informed consent for the use of the material for research
119 purposes.

120 2.2 Generation of iPSC lines

121 Reprogramming of all primary cell lines into iPSCs used in this study was performed by the Erasmus MC iPS
122 Core Facility. Primary cell lines were reprogrammed using the CytoTune™-iPS 2.0 Sendai Reprogramming
123 Kit (Thermo Fisher Scientific) based on a modified non-transmissible form of Sendai virus (SeV), which
124 contains reprogramming Yamanaka factors, OCT3/4, SOX2, KLF4, and C-MYC. The emerging iPSC colonies
125 were manually picked and expanded four to five weeks after transduction. The selection was based on
126 morphology. iPSCs were cultured in StemFlex™ medium (Gibco™) on Geltrex™ (Thermo Fisher Scientific)
127 coated plates at 37 °C/5% CO_2. iPSCs were passaged when they reached ~80% confluence using Versene
128 (Gibco™). Multiple clones per line were assessed for their karyotype, expression of endogenous

129 pluripotency factors, and three lineages (ectoderm, endoderm, and mesoderm) differentiation potential
130 following the procedures of the Erasmus MC iPS Core Facility.

131 2.3 Primary and secondary antibodies

132 The primary antibodies used in this study are listed in Supplementary Table 3. Alexa Fluor® 488 donkey
133 anti-goat/mouse/rabbit, Alexa Fluor® 594 donkey anti-mouse/rabbit, Alexa Fluor® 647 donkey anti-rabbit,
134 and Alexa Fluor® 647 goat anti-guinea pig (all from Jackson ImmunoResearch) have been used as secondary
135 antibodies for ICC experiments and microscopic analysis.

136 2.4 Characterization of iPSC lines with immunocytochemistry (ICC)

137 iPSCs grown on coverslips were fixed with 4% PFA for 15 min at room temperature (RT). Cells were washed
138 three times for 5 min with 1× PBS buffer. Next, cells were incubated with ice-cold methanol for 10 min and
139 washed one time with 1× PBS buffer. Subsequently, cells were permeabilized with 0.1% Triton-X100 (Sigma-
140 Aldrich) in 1× PBS buffer for 10 min. Cells were blocked in a blocking buffer containing 1% BSA (Sigma-
141 Aldrich) in 1× PBS-0.05% TWEEN® 20 (Sigma-Aldrich). Then, cells were incubated with the blocking buffer
142 containing primary antibody mixtures overnight at 4 °C. The next day, cells were washed three times for 5
143 min in 1× PBS-0.05% TWEEN® 20 buffer. Cells were then incubated with appropriate Alexa Fluor® secondary
144 antibodies (1:500 dilution) for 1 hour at RT. Cells were washed three times with 1× PBS-0.05% TWEEN® 20
145 buffer. Finally, coverslips were mounted with ProLong Gold with DAPI (Invitrogen). All stainings were
146 imaged with Leica SP5 AOBS confocal microscope. Each image was detected on the spectral PMT detector
147 with an HCX PL APO CS 40×/1.25 or HCX PL APO CS 63×/1.4 lens. Sections were irradiated with the following
148 lasers: 405 diode UV, argon laser, DPSS 561, and HeNe 633, depending on the fluorophore combination.
149 Scanning was performed at 400 Hz with a pixel size of 0.12 µm in the x, y-direction and 0.35 µm in the z-
150 direction. The pinhole size was set to one airy unit (AU).

151 2.5 Generation of neural progenitor cells

152 Neural progenitor cells were generated via inhibiting BMP and TGFβ signaling (dual-SMAD) and stimulation
153 of WNT and SHH signaling with small molecules according to published protocols (Grochowska et al., 2021;
154 Reinhardt et al., 2013) with few modifications. iPSCs grown in feeder-free conditions (StemFlex™ in
155 combination with Geltrex™) were detached from the plates using the Versene solution. Cells were
156 dissociated as clumps and plated on irradiated mouse embryonic fibroblasts (MEFs) in StemFlex™ medium
157 supplemented with 1× RevitaCell™ in a splitting ratio of 1:10. Cells were cultured at 37 °C/5% CO_2 until the
158 iPSC colonies reached the appropriate size in StemFlex™ media. Unwanted differentiations that arose
159 around the iPSC colonies were manually removed. When colonies populated ~70% of the culture dish, cells
160 were detached as clumps from the MEFs using Versene. Next, pieces of colonies were resuspended in
161 Human Embryonic Stem Cell medium [HESC, 80% DMEM/F-12, 20% KnockOut Serum Replacement, 1% L-
162 glutamine, 1% Penicillin-Streptomycin, 1% MEM-NEAA (all from Gibco™), and 0.0007% 2-β-
163 Mercaptoethanol (Sigma-Aldrich)] supplemented with 10 µM SB-431542 (SB, Tocris), 1 µM dorsomorphin
164 (DM, Abcam), 3 µM CHIR99021 (CHIR, Sigma), and 0.5 µM Purmorphamine (PMA, Stem Cell Technologies).
165 Clumps of cells were then transferred to 10 cm Petri dishes and cultured in suspension for six days on a
166 shaker at 80 RPM at 37 °C/5% CO_2. On day two, the medium was replaced by N2B27 medium [DMEM/F-
167 12– Neurobasal in 1:1 ratio, 1:100 B27 w/o Vitamin A, 1:200 N2, and 1% Penicillin-Streptomycin (all from
168 Gibco™)] supplemented with 10 µM SB, 1 µM DM, 3 µM CHIR, and 0.5 µM PMA. On day four, the medium
169 was changed to N2B27 medium supplemented with 3 µM CHIR, 0.5 µM PMA, and 150 µM Ascorbic Acid
170 (AA, Sigma). On day six, embryoid bodies showing a developing neuroepithelium were collected,
171 dissociated into smaller pieces, and plated on Corning® Matrigel® coated 12-well plates in N2B27 medium
172 supplemented with 3 µM CHIR, 200 µM AA, and 0.5 µM PMA at 37 °C/5% CO_2. Cell splits were usually
173 performed at 1:10 or 1:20 ratios. After passage five, 0.5 µM PMA was replaced by 0.5 µM Smoothened
174 Agonist (SAG, Abcam). Progenitors were passaged at least five times before astrocyte differentiations.
175 Progenitors can be expanded in bulk (up to passage 30) and frozen for long-term storage.

176 2.6 Differentiation of neural progenitors into ventral midbrain astrocytes

177 Neural progenitors that reached 70-80% confluence were dissociated into single cells using Accutase®
178 (Sigma-Aldrich). Cells were seeded in ultra-low-attachment 96-well U-bottom plates (BIOFLOAT™) at the
179 concentration of 15,000 cells per well in the N2B27 medium supplemented with 3 µM CHIR, 0.5 µM SAG,
180 and 200 µM AA. Before placing in the incubator, plates were spun down at 220 × g for 5 min. Cells were
181 cultured at 37 °C/5% CO_2. After three days, progenitor cells formed spheres of size around 300-400 µm. On
182 day three, the medium was replaced with a glial expansion medium containing DMEM/F-12, GlutaMAX,
183 1:50 B27 w/o Vitamin A, 1:100 N2, 1× MEM non-essential amino acids solution (NEAA), 1% Penicillin-
184 Streptomycin (all from Gibco™), freshly supplemented with 10 mM HEPES (Gibco™), 10 ng/mL EGF
185 (Peprotech), and FGF-2 (Peprotech). The medium was refreshed every other day. Cells were kept at 37
186 °C/5% CO_2. On day 17, the medium was switched to a glial induction medium containing DMEM/F-12,
187 GlutaMAX, 1:50 B27 w/o Vitamin A, 1:100 N2, 1× MEM non-essential amino acids solution (NEAA), 1%
188 Penicillin-Streptomycin (all from Gibco™), freshly supplemented with 10 mM HEPES (Gibco™), 10 ng/mL
189 EGF (Peprotech), and 10 ng/mL LIF (Peprotech). The medium was refreshed every other day until day 31.
190 Cells were kept at 37 °C/5% CO_2. On day 31, 15-20 spheres per line were carefully taken up and plated onto
191 one well of a 6-well plate coated with Corning® Matrigel®. Generally, spheres easily attach to the coated
192 surface. After attachment to the coated plates, the cells migrate out of the spheres. From day 31, the
193 cultures were maintained in glial maturation media containing DMEM/F-12, GlutaMAX, 1:50 B27 w/o
194 Vitamin A, 1:100 N2, 1× MEM non-essential amino acids solution (NEAA), 1% Penicillin-Streptomycin (all
195 from Gibco™), freshly supplemented with 10 mM HEPES (Gibco™), and 10 ng/mL CNTF (Peprotech). The
196 medium was refreshed every other day until day 59. From day 60 onwards, cells were refreshed every two
197 days with a glial maintenance medium containing DMEM/F-12, GlutaMAX, 1:50 B27 w/o Vitamin A, 1:100
198 N2, 1× MEM non-essential amino acids solution (NEAA), 1% Penicillin-Streptomycin, freshly supplemented
199 with 10 mM HEPES (all from Gibco™). From day 60, cells were used in the downstream functional

200 experiments. Cells were plated onto new Matrigel® coated wells at 50.000 cells/cm^2 when they
201 repopulated the entire well. Detailed cell culture media composition is listed in **Supplementary Table 2**.

202 2.7 Characterization of iPSC-derived progenitors and astrocytes with ICC

203 Cells were fixed with 4% PFA for 15 min at RT. Cells were washed three times for 5 min with 1× PBS buffer.
204 Next, cells were incubated in a staining buffer [50 mM Tris.HCl (pH 7.4), 0.9% NaCl, 0.25% gelatine, H_2O]
205 containing primary antibody mixtures overnight at 4 °C. The next day, cells were washed three times for 5
206 min in 1× PBS-0.1% TWEEN® 20 buffer. Cells were then incubated with appropriate Alexa Fluor® secondary
207 antibodies (1:200 dilution) for 1 hour at RT. Secondary antibodies were washed three times with 1× PBS-
208 0.1% TWEEN® 20 buffer. Finally, cells were mounted with ProLong Gold with DAPI (Invitrogen). Each image
209 was detected on the spectral PMT detector with an HCX PL APO CS 40×/1.25 or HCX PL APO CS 63×/1.4
210 lens. Sections were irradiated with the following lasers: 405 diode UV, argon laser, DPSS 561, and HeNe
211 633, depending on the fluorophore combination. Scanning was performed at 400 Hz with a pixel size of
212 0.12 µm in the x, y-direction and 0.35 µm in the z-direction. The pinhole size was set to 1 airy unit (AU). All
213 images were processed using Fiji (Fiji Is Just ImageJ) software (version 1.53c) (Schindelin et al., 2012). For
214 the quantitative characterization of neural progenitors and astrocytes, fluorescence-based thresholding
215 was applied for each marker. The cell was considered positive for a marker if its fluorescent signal was
216 above that threshold and within the boundaries of its belonging cell.

217 2.8 RNA extraction, sequencing, and alignment to reference genome

218 RNA was extracted from 14 iPSC-derived lines (eight progenitors and six astrocytes) generated from four
219 individuals (**Supplementary Table 4**). Cells were harvested and lysed with lysis buffer (1 mL RTL+10uL β-
220 mercaptoethanol) and scraped with a polypropylene disposable cell scraper. Cell lysates were transferred
221 to 1.5 mL tubes and vortexed to dissolve possible cell clumps. Samples were further processed using the
222 QIAGEN RNeasy® (GTIN 04053228006121, LOT 172019069, REF 74106) Mini Kit according to the

223 manufacturer's instructions. RNA fragments were analyzed using the RNA 6000 Nano Kit on an Agilent 2100
224 Bioanalyzer instrument (Agilent Technologies) to determine the RNA integrity number (RIN). About 1 µg
225 high-quality RNA sample (average RIN 9.9; **Supplementary Table 4**) from each sample was further processed
226 with the Illumina NEBNext Ultra II Directional RNA Library Prep Kit (NEB #E7760S/L) according to the
227 manufacturer's instructions. The generated libraries were sequenced on an Illumina NovaSeq6000 with
228 150 bp paired-end reads and an average of 60 million reads per sample (GenomeScan, Leiden,
229 Netherlands). RNA-seq data quality was assessed using fastqc v0.11.9 (Andrews, 2010) and summarized
230 using MultiQC v1.12 (Ewels et al., 2016). RNA-seq reads were aligned to the GRCh38 human reference
231 genome with STAR v2.7.10 (Dobin et al., 2013) run in multisample 2-pass mapping mode to improve the
232 detection of novel splice junctions. The counts of reads per gene were determined using FeatureCounts v2
233 (Liao et al., 2014) using ENSEMBL gene annotations v107.

234 2.9 Cell lines karyotyping

235 RNA-seq data were processed according to the GATK v4.2.5 guidelines (McKenna et al., 2010) to generate
236 a VCF with HaplotypeCaller. The possible presence of chromosomal multiplications was then assessed using
237 eSNP-Karyotyping (Weissbein et al., 2016) with the BAM and VCF in combination with dbSNP v155. As
238 previously described, the allelic ratio in sliding windows of 151 SNPs with a depth minimal allele frequency
239 above 0.2 and covered by more than 20 reads were compared with that of the rest of the genome.
240 Significant multiplications were identified as those with a false discovery rate < 0.05.

241 2.10 RNA-seq expression data analyses

242 Digital expression matrices of the analyzed cell lines were analyzed in R v4.2.1. Established cell-type specific
243 markers were obtained from BRETIGEA v.1.0.3 (McKenzie et al., 2018). Moreover, we used previously
244 described markers to characterize precursor cells and the maturity of the astrocytes (Sloan et al., 2017).
245 Low-expressed genes (<10 cumulative raw counts across all samples) were filtered out, resulting in 28,075

246 expressed genes. DESeq2 v1.36.0 (Love et al., 2014) was used to transform raw counts, assess sample-to-
247 sample distances and clustering via principal component analysis (PCA) on rlog-transformed data, and
248 perform differential expression analysis. The obtained *p*-values were corrected with the Benjamini-
249 Hochberg (BH) method (*BHp*-value), and differentially expressed genes (DEGs) were identified according to
250 the following thresholds: *BHp*-value< 0.05 and |fold change| > 1.5.

251 2.11 RNA-seq functional analysis

252 Gene set enrichment analysis (GSEA) was performed using the clusterProfiler v4.4.4 (Wu et al., 2021) and
253 org.Hs.eg.db v3.15.0 R packages with the Gene Ontology (GO) database. GO terms were filtered to include
254 sets comprised of 20 - 2,000 genes. The genes in our datasets were ranked in descending order by the
255 negative logarithm in base 10 of the adjusted *BHp*-value, multiplied for the sign of the fold change. All
256 resulting *p*-values were corrected using the BH method. A nervous system-centric analysis was conducted
257 extracting the 181 terms surviving out filtering criteria out of the 1,256 child terms of the nervous system
258 development set (GO:0007399).

259 2.12 Pro-inflammatory cytokine treatment: A1-like reactivity assay

260 We adapted the reactivity assay from Barbar et al (Barbar et al., 2020) to obtain an A1 reactive astrocyte
261 phenotype. Astrocytes were plated onto new Matrigel® coated wells at 50.000 cells/cm^2. Two days later,
262 astrocytes were treated with 30 ng/mL TNF-α (tumor necrosis factor α), 3 ng/mL IL-1α (interleukin 1α), and
263 400 ng/mL C1q (complement component 1, subcomponent q) for 24 hours. After 24 hours, cells were
264 collected, and the total RNA was isolated using the RNeasy Mini Kit (Qiagen) as recommended by the
265 manufacturer. For each sample, on-membrane DNase I (RNase-Free DNase Set, Qiagen) digestion was
266 performed according to the manufacturer's protocol. The integrity of the total RNA was assessed using
267 agarose gel stained with GelRed™ (Biotium) and spectrophotometric analysis using NanoDrop 2000/2000c.
268 Sharp, clear 28S and 18S rRNA bands without smearing and 260/280 values of ~2.0 indicated intact and

269 pure RNA. Next, 0.5 µg of the total RNA was converted into cDNA using the iScript cDNA Synthesis Kit (Bio-
270 Rad). qPCR was performed on CFX Opus 96 Real-Time PCR System (Bio-Rad) with ~0.1 µg cDNA per reaction.
271 The following cycling conditions were used: 3 min at 95 °C (initial denaturation), 40 cycles of 5 s at 95 °C,
272 and 30 s at 60 °C. Data analysis was performed using CFX Maestro software 2.3 (Bio-Rad). Briefly, the
273 normalized expression of each target gene was calculated using the delta–delta Cq method (Livak and
274 Schmittgen, 2001). Relative mRNA levels for *C3*, *LCN2*, *SERPINA3*, and *GFAP* were determined after
275 normalization to the geometric mean of the following housekeeping genes: *COPS5*, *CLK2*, and *RNF10*. All
276 assays, spanning at least one intron, were validated by demonstrating linearity over 3 orders of magnitude
277 and by observation of a single melt peak by plotting RFU data collected during a melt curve as a function of
278 temperature. Primers were adapted from previously published articles or designed using Primer3 v. 0.4.0
279 online tool (https://bioinfo.ut.ee/primer3-0.4.0/) and are listed in **Supplementary Table 5**.

280 2.13 Glutamate uptake assay

281 Astrocytes grown in 6-well plates were refreshed with glial maintenance media or glial maintenance media
282 supplemented with 100 µM L-Glutamic Acid (Tocris) for 3 h. The glutamate concentration in astrocyte
283 cultures was determined using the Glutamate Assay kit (Sigma-Aldrich, MAK004). To obtain cell
284 homogenates, astrocyte cultures were lifted with Accutase®, briefly centrifuged, and resuspended with 100
285 µL of the Glutamate Assay Buffer. Samples were centrifuged at 13,000 × g for 10 min to remove insoluble
286 material. Enzymatic reaction mixes were prepared by mixing Glutamate Assay Buffer, Developer, and
287 Enzyme Mix according to the manufacturer's specifications and were subsequently mixed with 50 µL of cell
288 homogenates and incubated for 30 min at 37 °C. Absorbance was measured at a 450 nm wavelength in a
289 Varioskan microtiter plate reader (ThermoFisher). Samples were run in duplicate and compared with the
290 Glutamate standard after subtracting the blank lacking the Enzyme Mix.

291 2.14 Intracellular Ca^{2+} imaging

292 Two days before live cell imaging, confluent astrocytes were seeded on Matrigel®-coated 24-mm round
293 glass coverslips in a 1:3 ratio. On the day of imaging, cells were treated with a loading solution of DMEM/F-
294 12 w/o Phenol red (Gibco™) containing 2 µM cell-permeant Fluo-4 acetoxymethyl ester (Fluo-4-AM,
295 Thermo Fisher) with the addition of the equal quantity (1:1 v/v) of 20% Pluronic F-127 (Thermo Fisher), to
296 assist in the dispersion of the nonpolar AM ester in the aqueous medium. After incubation with the loading
297 solution for 30 min at 37 °C, the astrocytes were washed thoroughly three times with DMEM/F-12 w/o
298 Phenol red to remove any dye non-specifically associated with the cell surface. Finally, coverslips were
299 mounted in live-cell imaging chambers and immediately transferred to a Leica SP5 AOBS inverted confocal
300 microscope equipped with a live-cell module maintaining a 37 °C, 5% CO_2, and >90% relative humidity
301 environment. After a 1-min time-lapse series acquisition, ATP solution (Sigma-Aldrich) was added to the
302 medium. The final concentration of ATP in the medium was 100 µM. The ATP was added carefully using a
303 conventional pipette, without touching the imaging chamber, to avoid movement artifacts and ensure that
304 the same field of view was imaged before and after the ATP application. Finally, a 10-min time-lapse series
305 were acquired to record the ATP-induced fluorescence. Series were recorded at 400 Hz with 1 frame per
306 second (fps) acquisition. Each frame was detected on a spectral PMT detector with an HCX PL APO CS
307 20×/0.7 DRY UV lens. Cells were irradiated with the argon laser.

308 2.15 Quantification of calcium imaging traces with deCLUTTER^{2+} pipeline

309 All images were processed using Fiji software (version 1.53c). Raw time-lapse imaging stacks (*x*, *y*, *t*) of
310 intracellular Ca^{2+} were first corrected for a drift using a *Correct 3D Drift* plug-in (Parslow et al., 2014). To
311 obtain individual Ca^{2+} traces, cells were segmented with a semi-automated segmentation strategy adapted
312 from a method described by Schwendy et al (Schwendy et al., 2019). To estimate cell borders, the local
313 maxima (mainly located in the cell nucleus) of each cell in a Z-projected image were determined to create
314 an inverted tile mask with one segmented particle (tile) per maximum. Next, another mask was made using
315 a Li background threshold method to select the total cell area in the image. In this case, the "leaky"

316 fluorescence from the FLUO-4-AM was exploited to identify all the cell bodies via a thresholding method.
317 A logical *XOR* operation using an *Image Calculator* was performed on both masks. To smooth the objects
318 and remove isolated pixels, erosion and dilation were performed using an *Open* function in the Binary
319 submenu. The remaining holes were filled using a *Fill Holes* function in the Binary submenu. Regions of
320 Interest (ROIs) were created using an *Analyze Particle* plug-in. Each ROI was manually inspected to ensure
321 that it defines only one cell. ROIs connected at one or two pixels were separated with the *Selection Brush*.
322 Lastly, mean grey values per time frame were calculated in each ROI. For each time point in each ROI, we
323 calculated the signal-to-baseline ratio of fluorescence F using the formula $\Delta \mathrm{F} = \frac{F - F_0}{F_0}$, where the baseline
324 F_0 is estimated as the average of the fluorescence levels of 20 time points before ATP addition. The traces
325 were visualized using a ggplot2 v3.3.6 and pheatmap v1.0.12 R packages.

326 To capture the time functions underlying the calcium influx behaviors observed in the astrocytes, we
327 employed functional principal component analysis (fPCA). With this technique, it is possible to analyze a
328 set of observations ordered in time, i.e., functions, and to identify the underlying eigenfunctions (ϕ) that
329 describe the shape of the data. Similarly to the principal components in PCA, ϕ are ranked by the amount
330 of variance they explain and can be used to reduce the dimensionality of the dataset. $\Delta F/F_0$ values from the
331 six cell lines were merged and analyzed with the fdapace v0.5.9 (Jane-Ling et al., 2016) R package. Next, we
332 selected the top ϕs explaining 95% of the variance in the data. We used them as an input for uniform
333 manifold approximation and projection (UMAP) onto two dimensions using the umap v0.2.9.0 R package.
334 Finally, we performed k-means clustering using the factoextra v1.0.7 0 R package and selected k = 3 using
335 the elbow plot method and visual evaluation of the UMAP plot.

336 2.16 Statistical analyses

337 Statistical analyses were carried out using GraphPad Prism 9 (San Diego, USA). Unpaired t-test was
338 performed for the analysis of the glutamate uptake assay. Two-way ANOVA with post hoc Tukey test were
339 applied to the immunocytochemistry of astrocytes. Effects with p-value < 0.05 were considered significant.

340 ## 3. Results

341 ### 3.1 Astrocytes are derived from ventral midbrain patterned progenitor cells

342 We developed a strategy to differentiate human-derived iPSCs into astrocytes by combining various steps
343 from previously described astrocyte differentiation protocols and the principles of astrocyte development
344 in vivo. First, we generated eight iPSC lines that formed compact colonies with well-defined edges and
345 expressed pluripotency markers, including NANOG, SSEA-4, OCT-4, and TRA-1-81 (**Supplementary Fig. 1A**).
346 Next, we generated neural progenitor cells patterned towards a ventral midbrain identity that are able to
347 also differentiate into dopaminergic neurons (**Supplementary Fig. 1B**, **1C**, and **1D**) as previously described
348 (Grochowska et al., 2021; Monzel et al., 2017; Quadri et al., 2018; Reinhardt et al., 2013; Vanhauwaert et
349 al., 2017). These progenitor lines expressed neural progenitor markers such as SOX2 and nestin but
350 remained undifferentiated, as demonstrated by low expression of the mature neuron marker MAP2
351 (**Supplementary Fig. 1D**).

352 In vivo, neural progenitors undergo many rounds of neurogenesis before committing to the glial fate (Miller
353 and Gauthier, 2007). Hence, we strived to accelerate gliogenesis in vitro by combining several well-
354 established approaches. It has been shown that culturing astrocytes in a three-dimensional matrix induces
355 the expression of astrocyte-specific genes and improves astrocyte maturity (Lattke et al., 2021). Therefore,
356 we aggregated progenitor cells to form floating spheres (**Fig. 1A, 1Bb, and 1Bc**). Next, we exposed the
357 spheres to basic fibroblast growth factor (bFGF) and epidermal growth factor (EGF) to mass amplify
358 progenitor cells. Consecutively, we added leukemia inhibitory factor (LIF) and EGF to accelerate glial
359 differentiation by the activation of the JAK-STAT signaling pathway (Bonni et al., 1997; Perriot et al., 2018)

360 (**Fig. 1A**). Finally, when astrocyte-enriched spheres were plated, astrocytes migrated radially out of the
361 spheres in the presence of ciliary neurotrophic factor (CNTF) for further maturation (**Fig. 1A** and **1Bd**). Out
362 of eight cell lines, two lines failed to attach firmly to the plates. Therefore, they were excluded from further
363 analyses. This procedure led to a proliferative population of astrocytes expressing key astrocyte markers,
364 including glial fibrillary acidic protein (GFAP), aquaporin 4 (AQP4), astrocytic precursor markers CD44, and
365 nestin in all human iPSC-derived astrocytes as demonstrated by ICC (**Fig. 1C**). On average, this protocol
366 yielded 82% of GFAP-expressing astrocytes at week 13 (**Fig. 1D**). The GFAP expression increased to 90%
367 after 20 weeks in culture (**Fig. 1E**). At both time points, there were significant differences detected in cell
368 composition between lines (**Fig. 1D** and **1E**). No evident contamination by neurons was found, as assessed
369 by immunostaining with an anti-MAP2 antibody, confirming the efficiency of this protocol in generating
370 highly enriched astrocyte populations (**Fig. 1C-E**).

371 3.2 Distinct expression profiles separate precursors and astrocytes

372 To investigate the molecular characteristics and whether the observed morphological changes were
373 consistent with changes in the transcriptional landscape, we sequenced RNA from eight progenitor and six
374 astrocyte lines. First, we employed eSNP-Karyotyping on the RNA-seq data to check for chromosomal
375 aberrations. No large chromosomal multiplication could be detected in any of the progenitor lines
376 (**Supplementary Fig. 2**). eSNP-Karyotyping revealed a chr2 multiplication in one of the astrocyte lines. Other
377 astrocyte lines showed patterns similar to the corresponding precursor lines. Hence, we excluded the D4-
378 c1 astrocyte line from the following transcriptomic analyses.

379 Next, we aimed to determine whether expression profiling could unbiasedly stratify the generated cell
380 lines. PCA analysis on the top 500 most variable genes revealed two well-distinct groups corresponding to
381 the two populations. PC1, capturing 82% of the variability in gene expression, clearly discriminated
382 between the two (**Fig. 2A**).

383 We assessed the expression of the top 10 markers selected from BRETIGEA encompassing six cell types
384 (astrocytes, endothelial cells, neurons, microglia, oligodendrocytes, and oligodendrocytes precursor cells)
385 and from literature for the progenitors to identify the cell lines. The precursors and the astrocytes
386 expressed the expected cell-type specific markers consistently. In contrast, lower-to-no expression of the
387 majority of markers of the other cell types could be detected (**Fig. 2B**). However, the astrocytes expressed
388 some of the markers of the precursor cells. For this reason, we assessed the maturity level of the generated
389 astrocytes using a list of markers for fetal and mature astrocytes (Sloan et al., 2017) (**Fig. 2C**). Compared to
390 the precursor cells, astrocytes expressed a high level of two of the mature astrocyte markers (*AQP4* and
391 *IGFBP7*). Lower expression levels of fetal astrocytes markers could still be detected in the astrocytes.

392 3.4 Genome-wide expression profiling confirms effective differentiation

393 We performed differential expression analysis on the RNA-seq data to identify the genes driving the
394 differences between the precursors and astrocytes we generated. A total of 13,452 DEGs was detected.
395 7,196 were upregulated in the astrocytes compared to the progenitors (**Fig. 2D**, **Supplementary Table 6**).
396 Among the top up-regulated genes, we found established astrocytic markers, including *GFAP* (log2FC 16.87
397 ± 0.55, *BHp*-value 3.84×10^{-201}) and *AQP4* (log2FC 14.07 ± 0.73, *BHp*-value 4.02×10^{-79}). Similarly, among
398 the top down-regulated genes, we identified genes related to the stemness and proliferative potential of
399 the precursor cells, including *LIN28A* (log2FC -16.51 ± 1.02, *BHp*-value 3.59×10^{-57}) and *PAX5* (log2FC -15.88
400 ± 1.37, *BHp*-value 1.07×10^{-29}).

401 We also assessed the effect of the differentiation at the pathway level by performing GSEA on the genes
402 ranked by the differential expression analysis statistics. 1,282 terms from the gene ontology biological
403 process category were significantly different between the two cell types, with 808 being upregulated in the
404 astrocytes confirming broad differences in the transcriptomes of the two lines (**Supplementary Table 7**). We
405 prioritized the nervous system development (GO:0007399) child terms from this category to focus on the

406 differentiation effect. Of the 181 terms passing our filtering criteria, 16 significantly differed between
407 astrocytes and precursors. The top significantly up-regulated term was astrocyte differentiation (NES =
408 1.86, *BHp*-value 6.16×10^{-4}), further supporting the directionality and effectiveness of the differentiation
409 protocol (**Fig. 2E, Supplementary Table 7**).

410 3.5 Astrocytes respond to pro-inflammatory cytokines and display a low extracellular glutamate uptake

411 Reactive astrocytes play an important role in the pathogenesis of many neurodegenerative diseases
412 (Escartin et al., 2021). To investigate this, several studies have modeled inflammation-stimulated reactivity
413 in iPSC-derived astrocytes (Barbar et al., 2020; Leng et al., 2022; Perriot et al., 2018; Roybon et al., 2013;
414 Santos et al., 2017; Tchieu et al., 2019; Tcw et al., 2017). We also characterized the transcriptomic profile
415 of our astrocytes stimulated with pro-inflammatory cytokines TNF-α, IL-1α, and C1q that drive an A1-like
416 reactive state (Liddelow et al., 2017) using qPCR. iPSC-derived astrocytes exhibited morphological changes
417 upon the cytokine treatment, including the remodeling of GFAP-positive intermediate filaments (**Fig. 3A**).
418 A proportion of treated astrocytes appeared to have more cellular processes containing GFAP intermediate
419 filaments and more intermediate filament branches than the untreated astrocytes (**Fig. 3A**, boxed areas).
420 Next, we assessed the expression of *C3*, *LCN2*, *SERPINA3*, and *GFAP* transcripts affected in astrocytes in
421 vivo and in vitro upon A1 stimulation (Barbar et al., 2020; Liddelow et al., 2017). TNF-α, IL-1α, and C1q
422 treated astrocytes showed strong upregulation of *C3*, *LCN2*, and *SERPINA3* mRNA transcripts as assessed
423 by the RT-qPCR (**Fig. 3B-D**). The levels of upregulation of *C3*, *LCN2,* and *SERPINA3* showed heterogeneous
424 responses across the different astrocyte lines. Strikingly, *GFAP* expression was downregulated in the
425 treated astrocytes across all cell lines (**Fig. 3E**). This contrasts with the changes in the astrocytic cytoskeleton
426 and hypertrophy we detected with GFAP immunocytochemistry in the treated astrocytes. Overall, we
427 observed similar expression patterns to previous in vitro and in vivo studies (Barbar et al., 2020; Liddelow
428 et al., 2017). These results show that the generated astrocytes are immunocompetent and respond to
429 inflammatory stimuli by changing their morphology and transcript expression.

430 We next tested another important astrocyte physiological function, the uptake of glutamate, which
431 prevents neuronal excitotoxicity in vivo (Verkhratsky and Nedergaard, 2018). All lines presented detectable
432 levels of intracellular glutamate in baseline conditions (average 5.47 ± 1.195 nmol). Five out of six astrocyte
433 lines showed a slight increase in the uptake of extracellular glutamate upon 3 h treatment (average 5.94 ±
434 1.113 nmol) (**Fig. 3F**). However, these findings were not significant in pooled testing (**3G**).

435 3.6 Fluoro-4-AM imaging confirms electrophysiological responsiveness of astrocytes and deCLUTTER^{2+}
436 pipeline reveals dominant profiles and clusters in calcium traces

437 Neurotransmitter-induced intracellular Ca^{2+} transients play a pivotal role in astrocyte functionality and have
438 been observed in vivo and ex vivo systems (Gorzo and Gordon, 2022; Lia et al., 2021). We thus wanted to
439 assess whether the generated astrocytes possessed a similar physiological property.

440 We used Fluo-4-AM cell loading coupled with ATP stimulation to analyze the calcium dynamics in the
441 astrocyte lines. We imaged all the cell lines and identified green-fluorescent ROIs in the somata using Fiji.
442 We selected 52 cells per line, resulting in a total of 312 cells across six cell lines. Heatmaps showed that the
443 different cell lines had a heterogeneous response to the ATP stimulus with a variable number of responsive
444 cells. These cells were characterized by distinct patterns with an average peak amplitude of 0.68 ± 0.57 $\frac{\Delta F}{F0}$
445 (**Fig. 4A**). Although to different extents, an increase in fluorescence upon the ATP stimulus was evident in
446 all cell lines.

447 To further characterize the ATP-response behavior, we developed a novel pipeline we named deCLUTTER^{2+}
448 that takes as input the Fluo-4-AM signal calculated with Fiji across the cells. Briefly, fPCA is applied to
449 perform dimension reduction and denoising (or deCLUTTER^{2+}) the signals. Next, clusters are identified using
450 k-means. Finally, UMAP is applied for visualization of the clusters (**Fig. 4B**).

451 Specifically, we applied fPCA to extract the main ϕs describing the dominant patterns of variability across
452 cell lines. The top 3 ϕs explained 83% of the variability in the Ca^{2+} traces (**Fig. 4C**). ϕ_1 (68% of the variability)
453 captured part of the stimulus-associated increase in fluorescence and then it remained nearly constant
454 with just a slow decrease. ϕ_2 (12% of the variability) encoded the sharp variation in fluorescence around
455 the ATP stimulus time point in responsive cells. Finally, ϕ_3 (2.6% of the variability) captured both the
456 variability around the ATP stimulus time point and another increase in fluorescence at about half the
457 imaging time course. To show the local and global structures in the cell lines with a 2D representation, we
458 constructed a lower dimensionality embedding with UMAP. We selected the top 22 ϕs, explaining 95% of
459 the variance in the Fluo-4-AM tracks. The different cell lines were admixed onto the UMAP plot, showing a
460 continuum with regions of higher density (**Fig. 4D**). In the case of the D2-derived lines, it was possible to
461 see an overlap that might be partially driven by a donor effect. We clustered the cell lines using k-means
462 clustering and obtained three distinct groups with a differential contribution from the various cell lines (**Fig.**
463 **4E**). The three clusters were characterized by different $\frac{\Delta F}{F0}$ profiles. The cell lines contributed a variable
464 number of cells to each cluster (**Fig. 4F**). Clusters 1 and 3 corresponded to low and non-responsive cells,
465 whereas cluster 2 contained cells highly responsive to the ATP stimulus.

466 ## 4. Discussion

467 iPSC-derived modeling is gaining momentum as a complementary method to study the properties of
468 human-derived cells under physiological and pathological conditions. However, specific protocols for the
469 generation of iPSC-derived ventral midbrain astrocytes to study the potential role of astrocytes in the non-
470 cell autonomous neurodegeneration observed in PD, have been lagging, and their morphological and
471 functional characterization are limited (**Supplementary Table 1**). In our study, we addressed some of these
472 limitations and generate midbrain-specified astrocytes by exploiting developmental events required for
473 astrogenesis.

474 Recent data indicates that ventral midbrain astrocytes differ from telencephalic astrocytes at the
475 physiological and transcriptomic levels (Siletti et al., 2022; Xin et al., 2019). However, what could be driving
476 these differences remains to be investigated. Several studies have proposed that such regional
477 heterogeneity of astrocytes arises early in development. The patterning along the neuraxis by sonic
478 hedgehog (SHH), fibroblast growth factors (FGFs), WNTs, and bone morphogenic factors (BMPs) leads to a
479 rostral-caudal and dorsal-ventral segmentation of the neuroepithelium into domains that give rise to
480 distinct subtypes of progenitors encoding regional information (Hochstim et al., 2008; Rowitch and
481 Kriegstein, 2010; Sardar et al., 2020; Tsai et al., 2012). Studies performed in various brain regions have
482 demonstrated that astrocytes and neurons derived from a common progenitor show a shared region-
483 specific molecular signature, which might act as a code for region-specific interactions (Herrero-Navarro et
484 al., 2021). Moreover, astrocytes and neurons derived from a common progenitor domain migrate radially
485 and share their final position (Herrero-Navarro et al., 2021; Torigoe et al., 2015). Hence, leveraging the
486 same progenitor pool for the generation of astrocytes and neurons in vitro might enable studying neuron-
487 astrocyte interactions of cells carrying a region-specific profile.

488 Although the developmental trajectory of the ventral midbrain astrocytes is poorly defined, we speculated
489 that the early patterning step would partially recapitulate the ventral midbrain ontogeny. Therefore, we
490 leveraged well-described patterning protocols using morphogens that specify the ventral midbrain identity
491 (Reinhardt et al., 2013). Importantly, the generated progenitor pool can also differentiate into vmDANs
492 (Grochowska et al., 2021; Reinhardt et al., 2013; Vanhauwaert et al., 2017). Our protocol resulted in a highly
493 pure population of cells expressing classical astrocyte markers. Furthermore, our astrocytes showed strong
494 transcriptomic evidence of the expected differentiation and expressed mature-astrocyte markers, including
495 AQP4, GFAP, and Connexin 43/GJA1. However, the low expression of some fetal-astrocyte markers and the
496 inefficient extracellular glutamate uptake suggest that subpopulations of lesser differentiated astrocytes
497 co-exist with more mature ones. On the other hand, the results of the glutamate uptake assay might have

498 been influenced by the presence of glutamate in the baseline culturing media warranting caution in the
499 interpretation of the data. The ratio of mature to immature cells might be further increased using
500 maturation-accelerating supplements like the ones reported in a recent preprint for iPSC-derived neurons
501 (Hergenreder et al., 2022). Unfortunately, the absence of a specific midbrain-astrocyte marker makes it
502 challenging to validate the ontogeny of the generated cell line. However, our astrocytes expressed high
503 levels of GFAP, in keeping with its high expression in subcortical regions, while lower expression is reported
504 in the cortical regions and the cerebellum (Siletti et al., 2022; Torres-Platas et al., 2016).

505 Genomic instability can have profound effects on cellular phenotypes, including growth speed,
506 differentiation potential, and resistance to stress (Weissbein et al., 2016). Therefore, we employed eSNP-
507 Karyotyping on the RNA-seq of all the cell lines and identified chromosomal aberrations in one of the
508 astrocyte lines (**Supplementary Fig. 2**). This highlights the importance of assessing for culturing-induced
509 chromosomal aberrations not only when iPSCs are generated but also after differentiation. This aspect has
510 surprisingly received little attention in previous literature despite the consequences that such events may
511 have on downstream analyses.

512 Next, we aimed to generate a model that recapitulates some of the functional properties of astrocytes. We
513 emphasize our findings from these functional assays, establishing iPSC-derived astrocyte cultures as a
514 platform for disease modeling. Recent research using post-mortem samples identified reactive astrocytes
515 in the midbrain of individuals with PD (Schonhoff et al., 2020). Therefore, we investigated the responses of
516 astrocytes to pro-inflammatory stimuli by treating the cells with TNF-α, IL-1α, and C1q that drive a reactive
517 phenotype (Escartin et al., 2021; Liddelow et al., 2017) . This assay has been widely used to study
518 neuroinflammation in vitro and in vivo (Barbar et al., 2020; Leng et al., 2022; Liddelow et al., 2017; Zhou et
519 al., 2019). Moreover, the morphology and transcriptomic profile of stimulated astrocytes have been well
520 characterized. Our protocol generated astrocytes that were immunocompetent. In particular, we observed
521 a strong upregulation of complement component 3 (C3), also found in the astrocytes residing in the

522 substantia nigra pars compacta (SNpc) of idiopathic PD cases (Liddelow et al., 2017). Moreover, we
523 observed similar expression patterns for *GFAP*, *LCN2*, and *SERPINA3* transcripts, which were in line with in
524 vivo studies and previously published iPSC-derived astrocyte protocols (Barbar et al., 2020; Liddelow et al.,
525 2017). Altogether, we characterized a cellular in vitro model that has the potential to be applied in
526 mechanistic studies on neuroinflammatory signaling in PD.

527 The effectiveness of our protocol is further supported by the data showing heterogeneous Ca^{2+} transients
528 in ventral midbrain astrocytes upon ATP treatment. These currents are known to have a critical impact on
529 neurotransmitter release (Bezzi and Volterra, 2001), synaptic transmission and plasticity (Di Castro et al.,
530 2011; Panatier et al., 2011), and even behavior and cognition (Kofuji and Araque, 2021; Nagai et al., 2021;
531 Santello et al., 2019) and are widely used as functional readouts in vivo and in vitro (Gorzo and Gordon,
532 2022; Lia et al., 2021). Importantly, calcium dysregulation is a potential mechanism for several genes
533 implicated in PD (Zaichick et al., 2017). Abnormal calcium signaling in the astrocytes might cause
534 dysfunction in dopaminergic neurons, activate microglia, and disrupt the blood brain barrier integrity,
535 therefore contributing to the pathological mechanisms seen in PD (Bancroft and Srinivasan, 2021). The
536 classical processing of calcium images from iPSC-derived astrocytes has encompassed visualization of the
537 transients via time-lapse imaging and traces. To better integrate the data from the different cell lines, we
538 developed the novel deCLUTTER^{2+} pipeline. deCLUTTER^{2+} can be used to perform semiautomatic
539 recognition of spontaneous or cue-dependent recurring patterns in fluorescence time-lapse imaging. Our
540 approach can handle variability and can be used to easily visualize local and global structures among the
541 analyzed cells. We anticipate that this approach could be used in the context of disease modeling to study
542 the association of specific cluster(s) to conditions.

543 In conclusion, we have generated ventral midbrain astrocytes that express astrocyte-specific markers and
544 recapitulate some of the physiological properties of in vivo ventral midbrain astrocytes. Our ventral
545 midbrain astrocyte model can also be integrated with neurons and other glial cell types, going beyond

546 traditional 2D co-culture systems (Majumdar et al., 2011; Park et al., 2018). Such neuron-glia interaction
547 paradigms might help elucidate the pathological processes observed in neurodegenerative diseases, for
548 example PD, and potentially pave the way toward disease-modifying treatments.

549 Acknowledgments

550 We thank Erasmus MC iPS Core Facility for providing the hiPSC lines and the Erasmus MC Optical Imaging
551 Center (OIC) members for their microscopy assistance.

552 **Author contributions:** M.M.G., F.F., D.N., and W.M. designed the experiments. M.M.G., A.C.M., D.N., Va.B.,
553 and G.J.B. performed the experiments. M.M.G., F.F., A.C.M., and D.N. performed data analysis. M.M.G.,
554 F.F., A.C.M., D.N., V.B., and W.M interpreted the data. M.M.G. and F.F. wrote the initial draft of the
555 manuscript. W.M. and V.B. conceived the study and supervised the experiments. All authors critically read
556 the manuscript and approved the final version.

557 **Funding:** This work was supported by research grants from the Stichting ParkinsonFonds (the
558 Netherlands) to V.B. (110875) and W.M. (110825) and from Alzheimer Nederland to V.B (WE.03-2019-
559 07).

560 **Data Availability Statement**: All analyses were conducted in R version v4.2.1 and ImageJ version 1.53c (Java
561 1.8.0_172 64-bit). Datasets are available upon reasonable request.

562 **Conflicts of Interest:** Dr. V. Bonifati receives research grants from the Stichting Parkinson Fonds (The
563 Netherlands) and from Alzheimer Nederland; he receives honoraria from Elsevier Ltd, for serving as co-
564 Editor-in-Chief of Parkinsonism & Related Disorders. The other authors declare no conflict of interest or
565 competing interests.

566 References

567 **Andrews, S.** (2010). FASTQC. A quality control tool for high throughput sequence data.
568 **Bancroft, E. A. and Srinivasan, R.** (2021). Emerging Roles for Aberrant Astrocytic Calcium Signals
569 in Parkinson's Disease. *Front Physiol* **12**, 812212.
570 **Bandopadhyay, R., Kingsbury, A. E., Cookson, M. R., Reid, A. R., Evans, I. M., Hope, A. D.,**
571 **Pittman, A. M., Lashley, T., Canet-Aviles, R., Miller, D. W. et al.** (2004a). The expression of DJ-1 (PARK7)
572 in normal human CNS and idiopathic Parkinson's disease. *Brain* **127**, 420-30.
573 **Bandopadhyay, R., Kingsbury, A. E., Cookson, M. R., Reid, A. R., Evans, I. M., Hope, A. D.,**
574 **Pittman, A. M., Lashley, T., Canet-Aviles, R., Miller, D. W. et al.** (2004b). The expression of DJ-1 (PARK7)
575 in normal human CNS and idiopathic Parkinson's disease. *Brain* **127**, 420-430.
576 **Barbar, L., Jain, T., Zimmer, M., Kruglikov, I., Sadick, J. S., Wang, M., Kalpana, K., Rose, I. V. L.,**
577 **Burstein, S. R., Rusielewicz, T. et al.** (2020). CD49f Is a Novel Marker of Functional and Reactive Human
578 iPSC-Derived Astrocytes. *Neuron* **107**, 436-453 e12.
579 **Batiuk, M. Y., Martirosyan, A., Wahis, J., de Vin, F., Marneffe, C., Kusserow, C., Koeppen, J.,**
580 **Viana, J. F., Oliveira, J. F., Voet, T. et al.** (2020). Identification of region-specific astrocyte subtypes at
581 single cell resolution. *Nat Commun* **11**, 1220.
582 **Bayraktar, O. A., Bartels, T., Holmqvist, S., Kleshchevnikov, V., Martirosyan, A., Polioudakis, D.,**
583 **Ben Haim, L., Young, A. M. H., Batiuk, M. Y., Prakash, K. et al.** (2020). Astrocyte layers in the mammalian
584 cerebral cortex revealed by a single-cell in situ transcriptomic map. *Nat Neurosci* **23**, 500-509.
585 **Beard, E., Lengacher, S., Dias, S., Magistretti, P. J. and Finsterwald, C.** (2021). Astrocytes as Key
586 Regulators of Brain Energy Metabolism: New Therapeutic Perspectives. *Front Physiol* **12**, 825816.
587 **Bezzi, P. and Volterra, A.** (2001). A neuron-glia signalling network in the active brain. *Curr Opin*
588 *Neurobiol* **11**, 387-94.
589 **Bonni, A., Sun, Y., Nadal-Vicens, M., Bhatt, A., Frank, D. A., Rozovsky, I., Stahl, N., Yancopoulos,**
590 **G. D. and Greenberg, M. E.** (1997). Regulation of gliogenesis in the central nervous system by the JAK-
591 STAT signaling pathway. *Science* **278**, 477-83.
592 **Booth, H. D. E., Hirst, W. D. and Wade-Martins, R.** (2017). The Role of Astrocyte Dysfunction in
593 Parkinson's Disease Pathogenesis. *Trends Neurosci* **40**, 358-370.
594 **Bugiani, M., Plug, B. C., Man, J. H. K., Breur, M. and van der Knaap, M. S.** (2022). Heterogeneity
595 of white matter astrocytes in the human brain. *Acta Neuropathol* **143**, 159-177.
596 **Chung, W. S., Allen, N. J. and Eroglu, C.** (2015). Astrocytes Control Synapse Formation, Function,
597 and Elimination. *Cold Spring Harb Perspect Biol* **7**, a020370.
598 **Dezonne, R. S., Stipursky, J., Araujo, A. P., Nones, J., Pavao, M. S., Porcionatto, M. and Gomes,**
599 **F. C.** (2013). Thyroid hormone treated astrocytes induce maturation of cerebral cortical neurons through
600 modulation of proteoglycan levels. *Front Cell Neurosci* **7**, 125.
601 **Di Castro, M. A., Chuquet, J., Liaudet, N., Bhaukaurally, K., Santello, M., Bouvier, D., Tiret, P. and**
602 **Volterra, A.** (2011). Local Ca2+ detection and modulation of synaptic release by astrocytes. *Nat Neurosci*
603 **14**, 1276-84.
604 **di Domenico, A., Carola, G., Calatayud, C., Pons-Espinal, M., Munoz, J. P., Richaud-Patin, Y.,**
605 **Fernandez-Carasa, I., Gut, M., Faella, A., Parameswaran, J. et al.** (2019). Patient-Specific iPSC-Derived
606 Astrocytes Contribute to Non-Cell-Autonomous Neurodegeneration in Parkinson's Disease. *Stem Cell*
607 *Reports* **12**, 213-229.
608 **Dobin, A., Davis, C. A., Schlesinger, F., Drenkow, J., Zaleski, C., Jha, S., Batut, P., Chaisson, M.**
609 **and Gingeras, T. R.** (2013). STAR: ultrafast universal RNA-seq aligner. *Bioinformatics* **29**, 15-21.

610 **Escartin, C., Galea, E., Lakatos, A., O'Callaghan, J. P., Petzold, G. C., Serrano-Pozo, A.,**
611 **Steinhäuser, C., Volterra, A., Carmignoto, G., Agarwal, A. et al.** (2021). Reactive astrocyte nomenclature,
612 definitions, and future directions. *Nature Neuroscience* **24**, 312-325.
613 **Ewels, P., Magnusson, M., Lundin, S. and Kaller, M.** (2016). MultiQC: summarize analysis results
614 for multiple tools and samples in a single report. *Bioinformatics* **32**, 3047-8.
615 **Gomes, F. C., Maia, C. G., de Menezes, J. R. and Neto, V. M.** (1999). Cerebellar astrocytes treated
616 by thyroid hormone modulate neuronal proliferation. *Glia* **25**, 247-55.
617 **Gomes, F. C., Sousa Vde, O. and Romao, L.** (2005). Emerging roles for TGF-beta1 in nervous
618 system development. *Int J Dev Neurosci* **23**, 413-24.
619 **Gonzalez-Reyes, R. E., Nava-Mesa, M. O., Vargas-Sanchez, K., Ariza-Salamanca, D. and Mora-**
620 **Munoz, L.** (2017). Involvement of Astrocytes in Alzheimer's Disease from a Neuroinflammatory and
621 Oxidative Stress Perspective. *Front Mol Neurosci* **10**, 427.
622 **Gorzo, K. A. and Gordon, G. R.** (2022). Photonics tools begin to clarify astrocyte calcium
623 transients. *Neurophotonics* **9**, 021907.
624 **Grochowska, M. M., Carreras Mascaro, A., Boumeester, V., Natale, D., Breedveld, G. J., Geut,**
625 **H., van Cappellen, W. A., Boon, A. J. W., Kievit, A. J. A., Sammler, E. et al.** (2021). LRP10 interacts with
626 SORL1 in the intracellular vesicle trafficking pathway in non-neuronal brain cells and localises to Lewy
627 bodies in Parkinson's disease and dementia with Lewy bodies. *Acta Neuropathol* **142**, 117-137.
628 **Hergenreder, E., Zorina, Y., Zhao, Z., Munguba, H., Calder, E. L., Baggiolini, A., Minotti, A. P.,**
629 **Walsh, R. M., Liston, C., Levitz, J. et al.** (2022). Combined small molecule treatment accelerates timing of
630 maturation in human pluripotent stem cell-derived neurons. *bioRxiv*, 2022.06.02.494616.
631 **Herrero-Navarro, A., Puche-Aroca, L., Moreno-Juan, V., Sempere-Ferrandez, A., Espinosa, A.,**
632 **Susin, R., Torres-Masjoan, L., Leyva-Diaz, E., Karow, M., Figueres-Onate, M. et al.** (2021). Astrocytes and
633 neurons share region-specific transcriptional signatures that confer regional identity to neuronal
634 reprogramming. *Sci Adv* **7**.
635 **Hochstim, C., Deneen, B., Lukaszewicz, A., Zhou, Q. and Anderson, D. J.** (2008). Identification of
636 positionally distinct astrocyte subtypes whose identities are specified by a homeodomain code. *Cell* **133**,
637 510-22.
638 **Ioannou, M. S., Jackson, J., Sheu, S. H., Chang, C. L., Weigel, A. V., Liu, H., Pasolli, H. A., Xu, C. S.,**
639 **Pang, S., Matthies, D. et al.** (2019). Neuron-Astrocyte Metabolic Coupling Protects against Activity-
640 Induced Fatty Acid Toxicity. *Cell* **177**, 1522-1535 e14.
641 **Jane-Ling, W., Jeng-Min, C. and Hans-Georg, M.** (2016). Functional Data Analysis. *Annual Review*
642 *of Statistics and Its Application* **3**, 257-295.
643 **Jessen, N. A., Munk, A. S., Lundgaard, I. and Nedergaard, M.** (2015). The Glymphatic System: A
644 Beginner's Guide. *Neurochem Res* **40**, 2583-99.
645 **Kim, J. M., Cha, S. H., Choi, Y. R., Jou, I., Joe, E. H. and Park, S. M.** (2016). DJ-1 deficiency impairs
646 glutamate uptake into astrocytes via the regulation of flotillin-1 and caveolin-1 expression. *Sci Rep* **6**,
647 28823.
648 **Kim, K. S., Kim, J. S., Park, J. Y., Suh, Y. H., Jou, I., Joe, E. H. and Park, S. M.** (2013). DJ-1 associates
649 with lipid rafts by palmitoylation and regulates lipid rafts-dependent endocytosis in astrocytes. *Hum Mol*
650 *Genet* **22**, 4805-17.
651 **Kofuji, P. and Araque, A.** (2021). Astrocytes and Behavior. *Annu Rev Neurosci* **44**, 49-67.
652 **Krencik, R., Weick, J. P., Liu, Y., Zhang, Z. J. and Zhang, S. C.** (2011). Specification of transplantable
653 astroglial subtypes from human pluripotent stem cells. *Nat Biotechnol* **29**, 528-34.
654 **Lanjewar, S. N. and Sloan, S. A.** (2021). Growing Glia: Cultivating Human Stem Cell Models of
655 Gliogenesis in Health and Disease. *Front Cell Dev Biol* **9**, 649538.

656 **Lattke, M., Goldstone, R., Ellis, J. K., Boeing, S., Jurado-Arjona, J., Marichal, N., MacRae, J. I.,**
657 **Berninger, B. and Guillemot, F.** (2021). Extensive transcriptional and chromatin changes underlie
658 astrocyte maturation in vivo and in culture. *Nat Commun* **12**, 4335.
659 **Leberbauer, C., Boulme, F., Unfried, G., Huber, J., Beug, H. and Mullner, E. W.** (2005). Different
660 steroids co-regulate long-term expansion versus terminal differentiation in primary human erythroid
661 progenitors. *Blood* **105**, 85-94.
662 **Leng, K., Rose, I. V. L., Kim, H., Xia, W., Romero-Fernandez, W., Rooney, B., Koontz, M., Li, E.,**
663 **Ao, Y., Wang, S. et al.** (2022). CRISPRi screens in human iPSC-derived astrocytes elucidate regulators of
664 distinct inflammatory reactive states. *Nat Neurosci*.
665 **Lia, A., Henriques, V. J., Zonta, M., Chiavegato, A., Carmignoto, G., Gomez-Gonzalo, M. and Losi,**
666 **G.** (2021). Calcium Signals in Astrocyte Microdomains, a Decade of Great Advances. *Front Cell Neurosci*
667 **15**, 673433.
668 **Liao, Y., Smyth, G. K. and Shi, W.** (2014). featureCounts: an efficient general purpose program for
669 assigning sequence reads to genomic features. *Bioinformatics* **30**, 923-30.
670 **Liddelow, S. A., Guttenplan, K. A., Clarke, L. E., Bennett, F. C., Bohlen, C. J., Schirmer, L., Bennett,**
671 **M. L., Munch, A. E., Chung, W. S., Peterson, T. C. et al.** (2017). Neurotoxic reactive astrocytes are induced
672 by activated microglia. *Nature* **541**, 481-487.
673 **Liu, L., Zhang, K., Sandoval, H., Yamamoto, S., Jaiswal, M., Sanz, E., Li, Z., Hui, J., Graham, B. H.,**
674 **Quintana, A. et al.** (2015). Glial lipid droplets and ROS induced by mitochondrial defects promote
675 neurodegeneration. *Cell* **160**, 177-90.
676 **Livak, K. J. and Schmittgen, T. D.** (2001). Analysis of relative gene expression data using real-time
677 quantitative PCR and the 2(-Delta Delta C(T)) Method. *Methods* **25**, 402-8.
678 **Love, M. I., Huber, W. and Anders, S.** (2014). Moderated estimation of fold change and dispersion
679 for RNA-seq data with DESeq2. *Genome Biol* **15**, 550.
680 **MacMahon Copas, A. N., McComish, S. F., Fletcher, J. M. and Caldwell, M. A.** (2021). The
681 Pathogenesis of Parkinson's Disease: A Complex Interplay Between Astrocytes, Microglia, and T
682 Lymphocytes? *Front Neurol* **12**, 666737.
683 **Majumdar, D., Gao, Y., Li, D. and Webb, D. J.** (2011). Co-culture of neurons and glia in a novel
684 microfluidic platform. *J Neurosci Methods* **196**, 38-44.
685 **McKenna, A., Hanna, M., Banks, E., Sivachenko, A., Cibulskis, K., Kernytsky, A., Garimella, K.,**
686 **Altshuler, D., Gabriel, S., Daly, M. et al.** (2010). The Genome Analysis Toolkit: a MapReduce framework
687 for analyzing next-generation DNA sequencing data. *Genome Res* **20**, 1297-303.
688 **McKenzie, A. T., Wang, M., Hauberg, M. E., Fullard, J. F., Kozlenkov, A., Keenan, A., Hurd, Y. L.,**
689 **Dracheva, S., Casaccia, P., Roussos, P. et al.** (2018). Brain Cell Type Specific Gene Expression and Co-
690 expression Network Architectures. *Sci Rep* **8**, 8868.
691 **Miller, F. D. and Gauthier, A. S.** (2007). Timing is everything: making neurons versus glia in the
692 developing cortex. *Neuron* **54**, 357-69.
693 **Miyazaki, I. and Asanuma, M.** (2020). Neuron-Astrocyte Interactions in Parkinson's Disease. *Cells*
694 **9**.
695 **Monzel, A. S., Smits, L. M., Hemmer, K., Hachi, S., Moreno, E. L., van Wuellen, T., Jarazo, J.,**
696 **Walter, J., Bruggemann, I., Boussaad, I. et al.** (2017). Derivation of Human Midbrain-Specific Organoids
697 from Neuroepithelial Stem Cells. *Stem Cell Reports* **8**, 1144-1154.
698 **Nagai, J., Yu, X., Papouin, T., Cheong, E., Freeman, M. R., Monk, K. R., Hastings, M. H., Haydon,**
699 **P. G., Rowitch, D., Shaham, S. et al.** (2021). Behaviorally consequential astrocytic regulation of neural
700 circuits. *Neuron* **109**, 576-596.
701 **Nones, J., Spohr, T. C. and Gomes, F. C.** (2012). Effects of the flavonoid hesperidin in cerebral
702 cortical progenitors in vitro: indirect action through astrocytes. *Int J Dev Neurosci* **30**, 303-13.

Oberheim, N. A., Takano, T., Han, X., He, W., Lin, J. H., Wang, F., Xu, Q., Wyatt, J. D., Pilcher, W., Ojemann, J. G. et al. (2009). Uniquely hominid features of adult human astrocytes. *J Neurosci* **29**, 3276-87.

Panatier, A., Vallee, J., Haber, M., Murai, K. K., Lacaille, J. C. and Robitaille, R. (2011). Astrocytes are endogenous regulators of basal transmission at central synapses. *Cell* **146**, 785-98.

Park, J., Wetzel, I., Marriott, I., Dréau, D., D'Avanzo, C., Kim, D. Y., Tanzi, R. E. and Cho, H. (2018). A 3D human triculture system modeling neurodegeneration and neuroinflammation in Alzheimer's disease. *Nat Neurosci* **21**, 941-951.

Parslow, A., Cardona, A. and Bryson-Richardson, R. J. (2014). Sample drift correction following 4D confocal time-lapse imaging. *J Vis Exp*.

Perriot, S., Mathias, A., Perriard, G., Canales, M., Jonkmans, N., Merienne, N., Meunier, C., El Kassar, L., Perrier, A. L., Laplaud, D. A. et al. (2018). Human Induced Pluripotent Stem Cell-Derived Astrocytes Are Differentially Activated by Multiple Sclerosis-Associated Cytokines. *Stem Cell Reports* **11**, 1199-1210.

Pestana, F., Edwards-Faret, G., Belgard, T. G., Martirosyan, A. and Holt, M. G. (2020). No Longer Underappreciated: The Emerging Concept of Astrocyte Heterogeneity in Neuroscience. In *Brain Sciences*, vol. 10.

Qiao, C., Yin, N., Gu, H. Y., Zhu, J. L., Ding, J. H., Lu, M. and Hu, G. (2016). Atp13a2 Deficiency Aggravates Astrocyte-Mediated Neuroinflammation via NLRP3 Inflammasome Activation. *CNS Neurosci Ther* **22**, 451-60.

Quadri, M., Mandemakers, W., Grochowska, M. M., Masius, R., Geut, H., Fabrizio, E., Breedveld, G. J., Kuipers, D., Minneboo, M., Vergouw, L. J. M. et al. (2018). LRP10 genetic variants in familial Parkinson's disease and dementia with Lewy bodies: a genome-wide linkage and sequencing study. *Lancet Neurol* **17**, 597-608.

Reinhardt, P., Glatza, M., Hemmer, K., Tsytsyura, Y., Thiel, C. S., Hoing, S., Moritz, S., Parga, J. A., Wagner, L., Bruder, J. M. et al. (2013). Derivation and expansion using only small molecules of human neural progenitors for neurodegenerative disease modeling. *PLoS One* **8**, e59252.

Rowitch, D. H. and Kriegstein, A. R. (2010). Developmental genetics of vertebrate glial-cell specification. *Nature* **468**, 214-22.

Roybon, L., Lamas, N. J., Garcia, A. D., Yang, E. J., Sattler, R., Lewis, V. J., Kim, Y. A., Kachel, C. A., Rothstein, J. D., Przedborski, S. et al. (2013). Human stem cell-derived spinal cord astrocytes with defined mature or reactive phenotypes. *Cell Rep* **4**, 1035-1048.

Santello, M., Toni, N. and Volterra, A. (2019). Astrocyte function from information processing to cognition and cognitive impairment. *Nat Neurosci* **22**, 154-166.

Santos, R., Vadodaria, K. C., Jaeger, B. N., Mei, A., Lefcochilos-Fogelquist, S., Mendes, A. P. D., Erikson, G., Shokhirev, M., Randolph-Moore, L., Fredlender, C. et al. (2017). Differentiation of Inflammation-Responsive Astrocytes from Glial Progenitors Generated from Human Induced Pluripotent Stem Cells. *Stem Cell Reports* **8**, 1757-1769.

Sardar, D., Cheng, Y.-T., Szewczyk, L. M., Deneen, B. and Molofsky, A. V. (2020). Chapter 32 - Mechanisms of astrocyte development. In *Patterning and Cell Type Specification in the Developing CNS and PNS (Second Edition)*, (eds J. Rubenstein P. Rakic B. Chen and K. Y. Kwan), pp. 807-827: Academic Press.

Scheibye-Knudsen, M., Fang, E. F., Croteau, D. L., Wilson, D. M., 3rd and Bohr, V. A. (2015). Protecting the mitochondrial powerhouse. *Trends Cell Biol* **25**, 158-70.

Schindelin, J., Arganda-Carreras, I., Frise, E., Kaynig, V., Longair, M., Pietzsch, T., Preibisch, S., Rueden, C., Saalfeld, S., Schmid, B. et al. (2012). Fiji: an open-source platform for biological-image analysis. *Nat Methods* **9**, 676-82.

Schonhoff, A. M., Williams, G. P., Wallen, Z. D., Standaert, D. G. and Harms, A. S. (2020). Innate and adaptive immune responses in Parkinson's disease. *Prog Brain Res* **252**, 169-216.

Schwendy, M., Unger, R. E., Bonn, M. and Parekh, S. H. (2019). Automated cell segmentation in FIJI(R) using the DRAQ5 nuclear dye. *BMC Bioinformatics* **20**, 39.

Siletti, K., Hodge, R., Mossi Albiach, A., Hu, L., Lee, K. W., Lönnerberg, P., Bakken, T., Ding, S.-L., Clark, M., Casper, T. et al. (2022). Transcriptomic diversity of cell types across the adult human brain. *bioRxiv*, 2022.10.12.511898.

Sloan, S. A., Darmanis, S., Huber, N., Khan, T. A., Birey, F., Caneda, C., Reimer, R., Quake, S. R., Barres, B. A. and Pasca, S. P. (2017). Human Astrocyte Maturation Captured in 3D Cerebral Cortical Spheroids Derived from Pluripotent Stem Cells. *Neuron* **95**, 779-790 e6.

Sofroniew, M. V. and Vinters, H. V. (2010). Astrocytes: biology and pathology. *Acta Neuropathol* **119**, 7-35.

Strokin, M., Seburn, K. L., Cox, G. A., Martens, K. A. and Reiser, G. (2012). Severe disturbance in the Ca2+ signaling in astrocytes from mouse models of human infantile neuroaxonal dystrophy with mutated Pla2g6. *Hum Mol Genet* **21**, 2807-14.

Tchieu, J., Calder, E. L., Guttikonda, S. R., Gutzwiller, E. M., Aromolaran, K. A., Steinbeck, J. A., Goldstein, P. A. and Studer, L. (2019). NFIA is a gliogenic switch enabling rapid derivation of functional human astrocytes from pluripotent stem cells. *Nat Biotechnol* **37**, 267-275.

Tcw, J., Wang, M., Pimenova, A. A., Bowles, K. R., Hartley, B. J., Lacin, E., Machlovi, S. I., Abdelaal, R., Karch, C. M., Phatnani, H. et al. (2017). An Efficient Platform for Astrocyte Differentiation from Human Induced Pluripotent Stem Cells. *Stem Cell Reports* **9**, 600-614.

Torigoe, M., Yamauchi, K., Zhu, Y., Kobayashi, H. and Murakami, F. (2015). Association of astrocytes with neurons and astrocytes derived from distinct progenitor domains in the subpallium. *Sci Rep* **5**, 12258.

Torres-Platas, S. G., Nagy, C., Wakid, M., Turecki, G. and Mechawar, N. (2016). Glial fibrillary acidic protein is differentially expressed across cortical and subcortical regions in healthy brains and downregulated in the thalamus and caudate nucleus of depressed suicides. *Mol Psychiatry* **21**, 509-15.

Tsai, H. H., Li, H., Fuentealba, L. C., Molofsky, A. V., Taveira-Marques, R., Zhuang, H., Tenney, A., Murnen, A. T., Fancy, S. P., Merkle, F. et al. (2012). Regional astrocyte allocation regulates CNS synaptogenesis and repair. *Science* **337**, 358-62.

van den Akker, E., Satchwell, T. J., Pellegrin, S., Daniels, G. and Toye, A. M. (2010). The majority of the in vitro erythroid expansion potential resides in CD34(-) cells, outweighing the contribution of CD34(+) cells and significantly increasing the erythroblast yield from peripheral blood samples. *Haematologica* **95**, 1594-8.

Vanhauwaert, R., Kuenen, S., Masius, R., Bademosi, A., Manetsberger, J., Schoovaerts, N., Bounti, L., Gontcharenko, S., Swerts, J., Vilain, S. et al. (2017). The SAC1 domain in synaptojanin is required for autophagosome maturation at presynaptic terminals. *Embo J* **36**, 1392-1411.

Verkhratsky, A. and Nedergaard, M. (2018). Physiology of Astroglia. *Physiol Rev* **98**, 239-389.

Weissbein, U., Schachter, M., Egli, D. and Benvenisty, N. (2016). Analysis of chromosomal aberrations and recombination by allelic bias in RNA-Seq. *Nat Commun* **7**, 12144.

Wu, T., Hu, E., Xu, S., Chen, M., Guo, P., Dai, Z., Feng, T., Zhou, L., Tang, W., Zhan, L. et al. (2021). clusterProfiler 4.0: A universal enrichment tool for interpreting omics data. *The Innovation* **2**, 100141.

Xin, W., Schuebel, K. E., Jair, K. W., Cimbro, R., De Biase, L. M., Goldman, D. and Bonci, A. (2019). Ventral midbrain astrocytes display unique physiological features and sensitivity to dopamine D2 receptor signaling. *Neuropsychopharmacology* **44**, 344-355.

Yang, Y., Song, J. J., Choi, Y. R., Kim, S. H., Seok, M. J., Wulansari, N., Darsono, W. H. W., Kwon, O. C., Chang, M. Y., Park, S. M. et al. (2022). Therapeutic functions of astrocytes to treat alpha-synuclein pathology in Parkinson's disease. *Proc Natl Acad Sci U S A* **119**, e2110746119.

Yun, S. P., Kam, T. I., Panicker, N., Kim, S., Oh, Y., Park, J. S., Kwon, S. H., Park, Y. J., Karuppagounder, S. S., Park, H. et al. (2018). Block of A1 astrocyte conversion by microglia is neuroprotective in models of Parkinson's disease. *Nat Med* **24**, 931-938.

Zaichick, S. V., McGrath, K. M. and Caraveo, G. (2017). The role of Ca(2+) signaling in Parkinson's disease. *Dis Model Mech* **10**, 519-535.

Zhou, Q., Viollet, C., Efthymiou, A., Khayrullina, G., Moritz, K. E., Wilkerson, M. D., Sukumar, G., Dalgard, C. L. and Doughty, M. L. (2019). Neuroinflammatory astrocytes generated from cord blood-derived human induced pluripotent stem cells. *Journal of Neuroinflammation* **16**, 164.

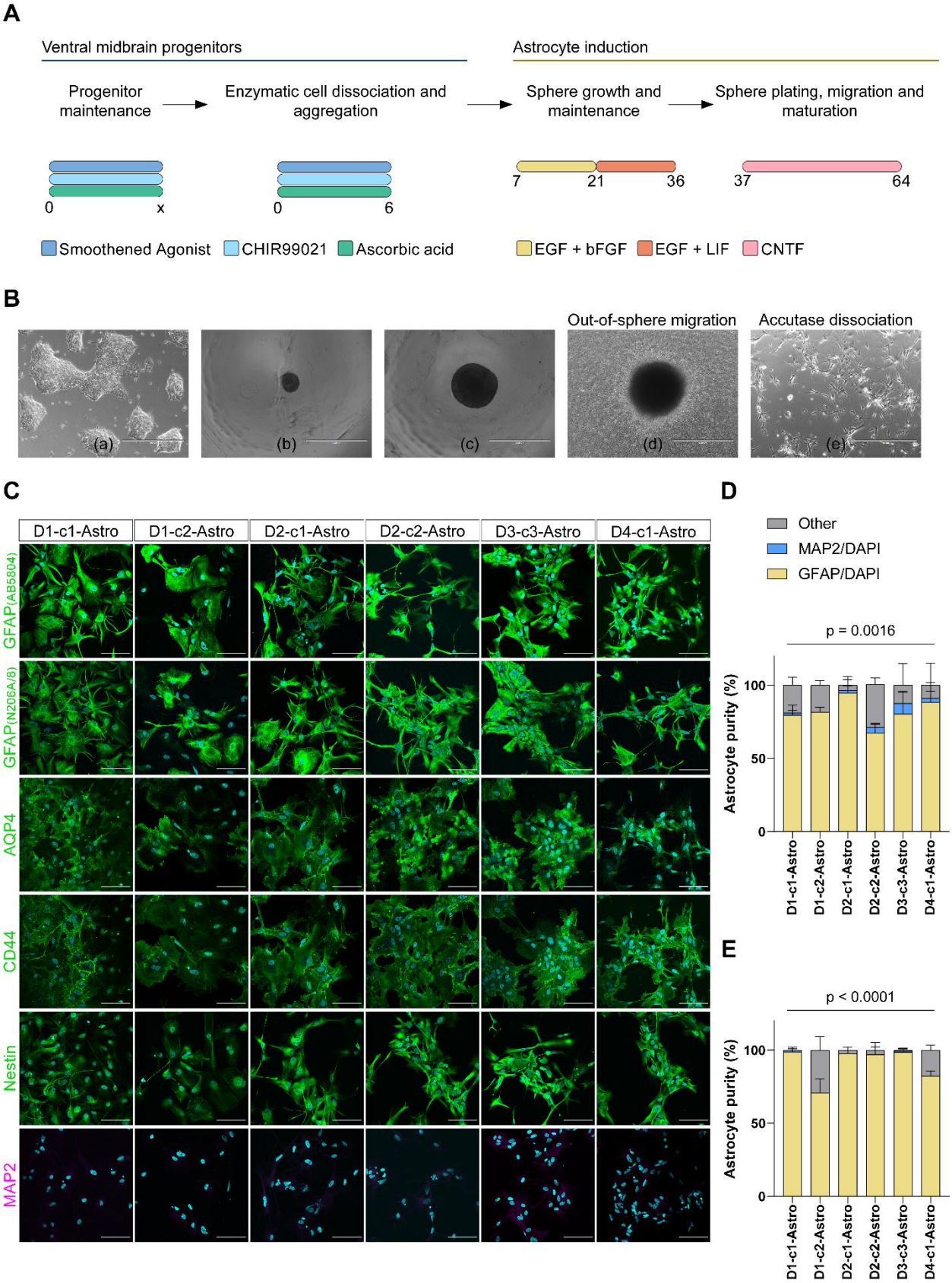
A
Ventral midbrain progenitors
Astrocyte induction
Progenitor maintenance
Enzymatic cell dissociation and aggregation
Sphere growth and maintenance
Sphere plating, migration and maturation
0
x
0
6
7
21
36
37
64
Smoothened Agonist
CHIR99021
Ascorbic acid
EGF + bFGF
EGF + LIF
CNTF
B
Out-of-sphere migration
Accutase dissociation
(a)
(b)
(c)
(d)
(e)
C
D1-c1-Astro
D1-c2-Astro
D2-c1-Astro
D2-c2-Astro
D3-c3-Astro
D4-c1-Astro
GFAP(AB5804)
GFAP(N206A/8)
AQP4
CD44
Nestin
MAP2
D
Other
MAP2/DAPI
GFAP/DAPI
p = 0.0016
Astrocyte purity (%)
100
50
0
D1-c1-Astro
D1-c2-Astro
D2-c1-Astro
D2-c2-Astro
D3-c3-Astro
D4-c1-Astro
E
p < 0.0001
Astrocyte purity (%)
100
50
0
D1-c1-Astro
D1-c2-Astro
D2-c1-Astro
D2-c2-Astro
D3-c3-Astro
D4-c1-Astro

807

808 **Fig. 1** Generation and immunocytochemical characterization of astrocytes derived from ventral midbrain
809 patterned progenitors. **A.** Schematic of the astrocyte differentiation protocol depicting the major steps with
810 the accompanying supplements. **B.** Representative bright field images of various cell morphologies at
811 different culturing steps during differentiation. Ventral midbrain progenitors (a) were seeded in low
812 attachment plates to form spheres (b). Spheres were cultured for several weeks in EGF/bFGF or EGF/LIF-
813 containing media (c). Spheres were plated and further differentiated with CNTF (d). Once matured,
814 astrocytes were enzymatically dissociated and used for downstream assays (e). **C.** Representative ICC
815 images of 20 weeks old astrocytes from six lines staining positive for general astrocyte markers GFAP and
816 AQP4, for astrocytic precursor markers CD44 and nestin, and staining negative for the mature neuron
817 marker MAP2. Scale bars, 100 µm. Nuclei were counterstained with DAPI (cyan). Astrocyte cultures mainly
818 comprise GFAP-positive cells at 13 (**D**) and 20 weeks (**E**). The number of independent differentiations per
819 line = 2. Two-way ANOVA, interaction *p*-value

820

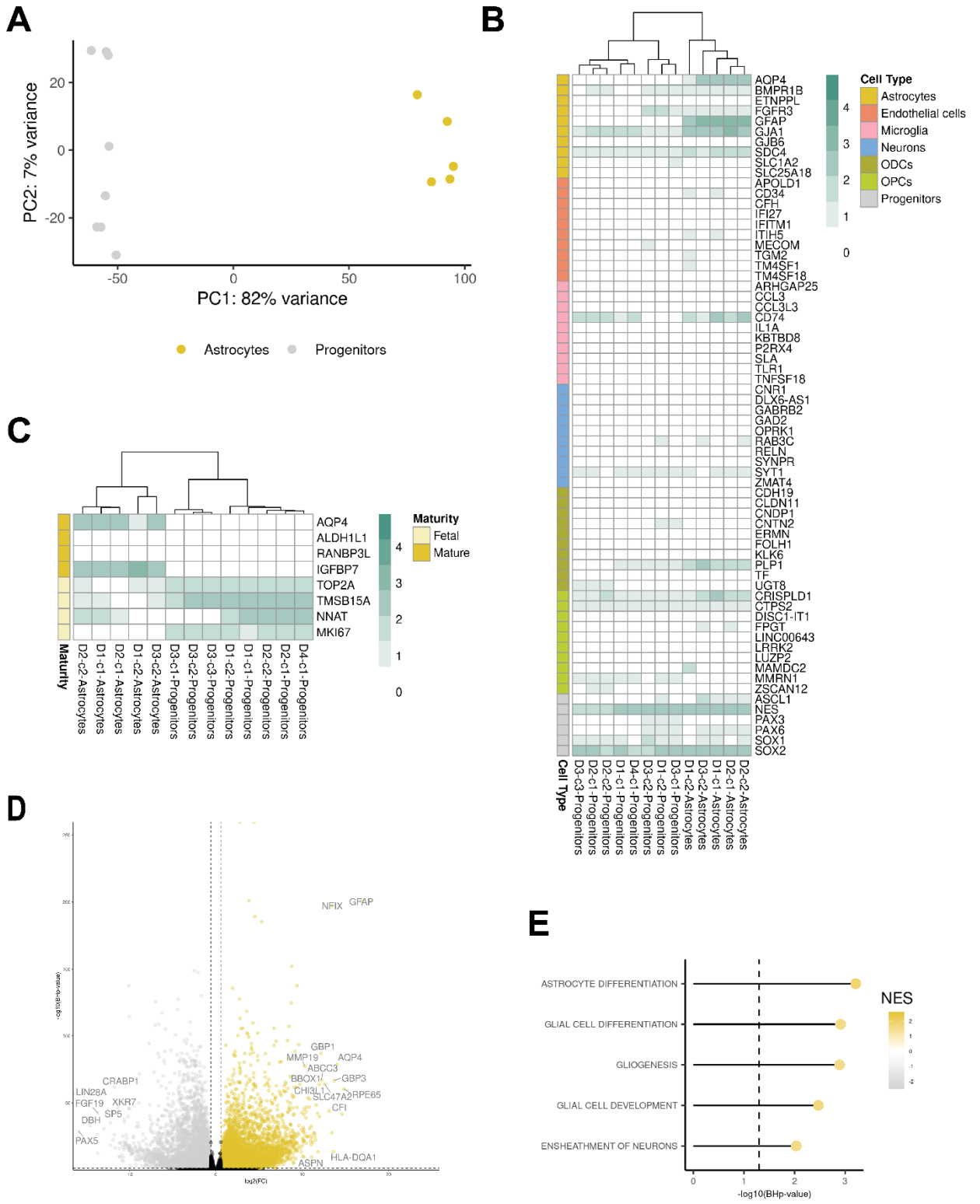

821

822 **Fig. 2** Transcriptomic characterization of progenitors and astrocytes. **A.** PCA plot showing line clustering

823 conducted on top 500 variable genes. **B.** Heatmap showing the level of expression as $\log_{10}$(FPKM+1) of top

824 10 BRETIGEA and literature-described markers for brain cell types. **C.** Heatmap showing the level of
825 expression as $\log_{10}$(FPKM+1) of literature-derived fetal and mature astrocyte markers. **D.** Volcano plot
826 showing significantly upregulated (yellow) and downregulated (grey) genes in the astrocyte lines compared
827 to the progenitor lines. **E.** Lollipop plot showing top 5 (ordered by *BHp*-value) significantly enriched gene
828 ontology biological processes among the nervous system development (GO:0007399) child terms

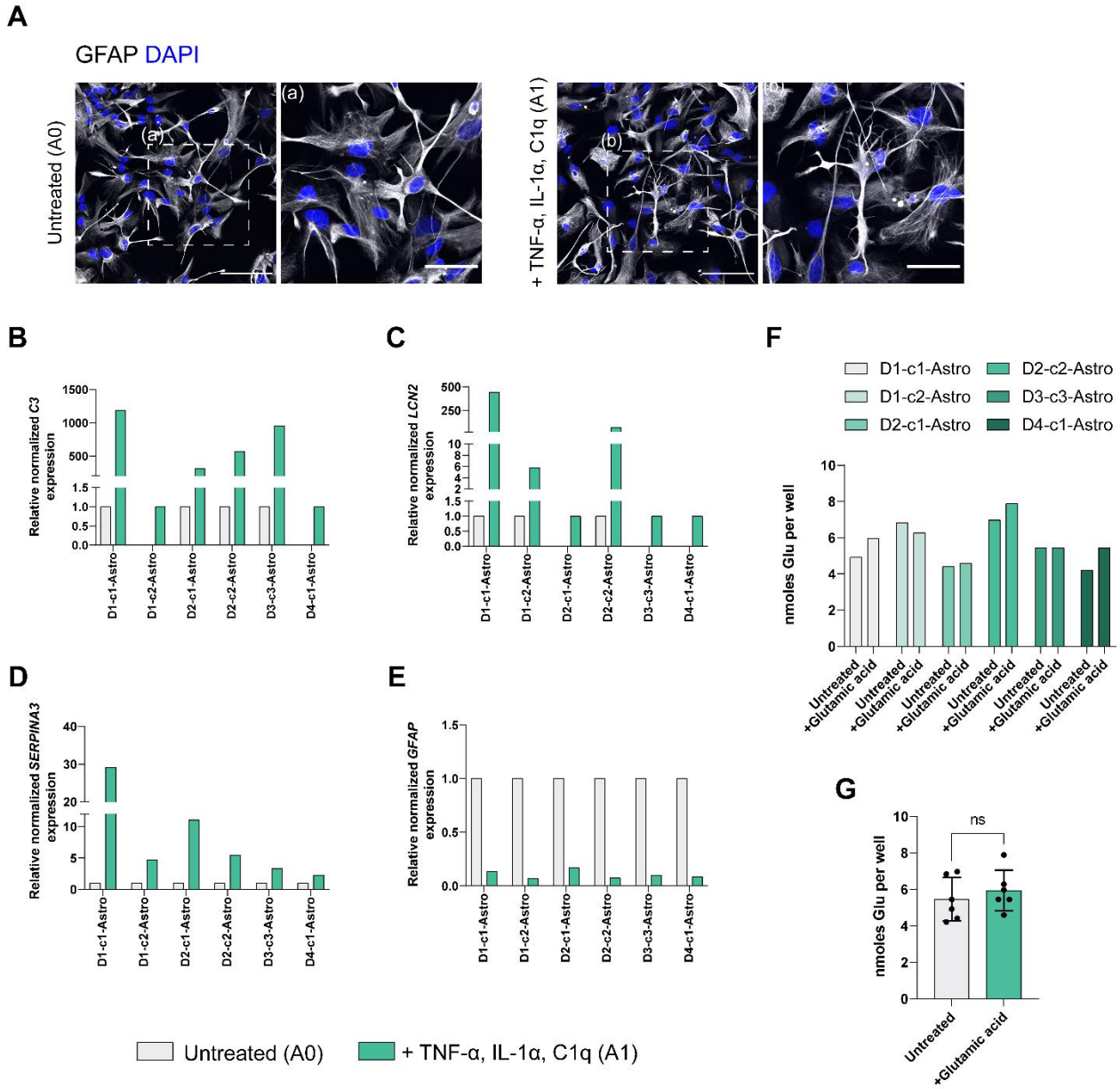

Fig. 3 Functional characterization of astrocytes. **A.** Representative ICC images showing GFAP (grey) expression in astrocytes upon stimulation with TNF-α, IL-1α, and C1q. Nuclei were counterstained with DAPI (blue). White dashed boxes indicate the magnified images (a, b) to highlight changes in morphology. Scale bars, 100 µm and 50 µm. **B-E**. 20 weeks old astrocytes upregulate reactive astrocyte-markers *C3* (**B**), *LCN2* (**C**), *SERPINA3* (**D**), and *GFAP* (**E**) upon TNF- α, IL-1α, and C1q treatment. Bar charts depict RT-qPCR analysis. Data represent the mean of relative normalized mRNA expression from three technical replicates.

836 *CLK2*, *COPS5*, and *RNF10* were used as housekeeping genes. **F**. Glutamate uptake analysis on 20 weeks
837 astrocytes. Bar graphs show nmoles of glutamate taken up by each astrocyte line after incubation with 100
838 µM glutamate for 3 h compared with untreated wells. Data represent the mean nmoles from two technical
839 replicates. **G.** Pooled results from **F**. Each dot represents an astrocyte line. Unpaired t-test; ns, not
840 significant

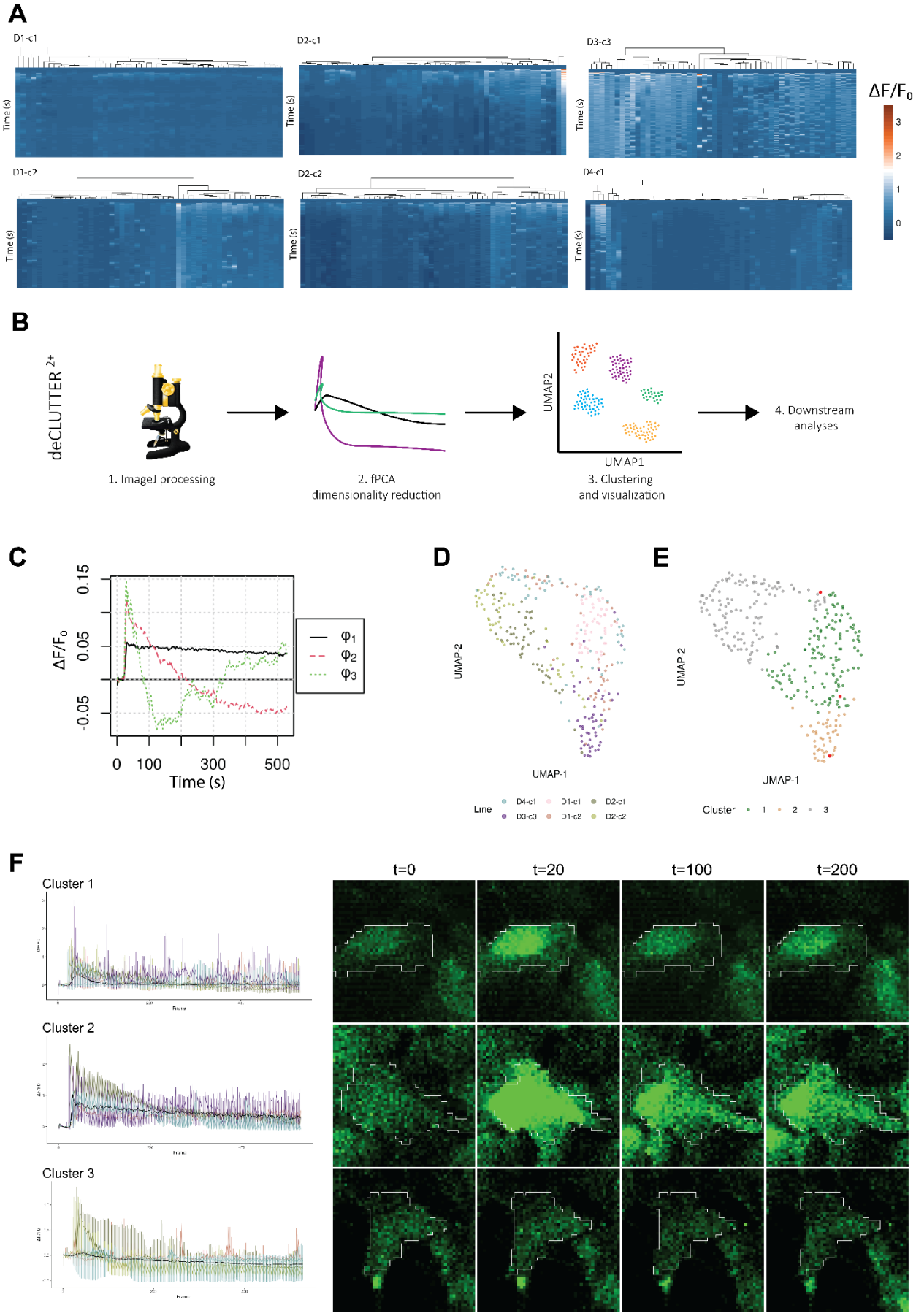
A
D1-c1
D2-c1
D3-c3
D1-c2
D2-c2
D4-c1
Time (s)
ΔF/F0
3
2
1
0
B
deCLUTTER 2+
1. ImageJ processing
2. fPCA
dimensionality reduction
UMAP2
UMAP1
3. Clustering
and visualization
4. Downstream
analyses
C
ΔF/F0
0.15
0.05
-0.05
0
100
300
500
Time (s)
φ1
φ2
φ3
D
UMAP-2
UMAP-1
Line
D4-c1
D1-c1
D2-c1
D3-c3
D1-c2
D2-c2
E
UMAP-2
UMAP-1
Cluster
1
2
3
F
Cluster 1
Cluster 2
Cluster 3
t=0
t=20
t=100
t=200

841

842 **Fig. 4** Characterization of ATP-induced Ca^{2+} transients in astrocytes. **A.** Heatmaps showing normalized $\Delta F/F_0$

843 values for the randomly selected cells for each cell line (n = 52). **B**. Schematic overview of deCLUTTER^{2+}

844 pipeline. **C.** fPCA top 3 eigenfunctions extracted from the $\Delta F/F_0$ across the cell lines. **D.** UMAP plot showing

845 astrocyte lines spread. **E.** UMAP plot showing clustering of the cells into the three k-means clusters. **F.** $\Delta F/F_0$

846 profiles of the three defined clusters along the imaging time course. Tracks are colored by cell line, and the

847 median $\Delta F/F_0$ is highlighted in black. Representative images of the three clusters sampled at time points

848 t=0, 20, 100, 200 s. The randomly selected cells are highlighted in red in Fig. 4D